metals

MDPI

Article

Effect of Heat Treatment on Tribological Behavior of Cr12Mo1V1Co Steel

Jue Wang [1,2,*], Yikai Guo [1], Hui Guo [1], Yuting Zhang [1] and Bin Feng [3]

[1] School of Materials Science and Engineering, Nanjing Institute of Technology, Nanjing 211167, China; wawzh12138@163.com (Y.G.); m13376090445@163.com (H.G.); 19895291860@163.com (Y.Z.)
[2] Jiangsu Key Laboratory of Advanced Structural Materials and Application Technology, Nanjing 211167, China
[3] Xinyuan Roller Industry Company Limited, Yixing 214253, China; 17768327638@163.com
* Correspondence: jue_wang@njit.edu.cn

Abstract

Relationships among processing, microstructure, and properties of Cr12Mo1V1Co steel under various quenching and tempering conditions were systematically investigated, with particular emphasis on tribological behavior. The microstructural evolution during heat treatment was characterized by optical microscopy, scanning electron microscopy, X-ray diffraction, and thermodynamic calculations. Reciprocating wear tests were performed with wear-scar morphologies analyzed using a three-dimensional optical profiler. The results reveal that the dominant wear mechanisms of Cr12Mo1V1Co steel are abrasive wear, oxidative wear, and fatigue wear under the present experimental conditions. Hardness represents the primary factor controlling the wear rate. High-hardness specimens deliver superior resistance to plastic deformation, which provides sufficient mechanical support for the oxide layer. This minimizes deformation within both the oxide film and the matrix during reciprocating friction, suppresses oxide spallation and mitigates abrasive, oxidative, and fatigue wear. The fracture and pull-out of large irregular M_7C_3 carbides constitute another important wear mechanism, and the associated carbide-originated wear can be alleviated via carbide edge dissolution triggered by elevated quenching temperatures. Considering both critical factors, specimens after 1100 °C quenching + 480 °C tempering and 1120 °C quenching + 500 °C tempering achieve optimal wear resistance among the investigated heat treatments under the present testing conditions.

Keywords: Cr12Mo1V1Co steel; wear mechanism; hardness; secondary quenching; irregular carbides

1. Introduction

Currently, the thickness of grain-oriented silicon steel strips for transformer cores has been reduced to under 0.18 mm to meet the core loss requirement (P1.7/50 < 0.6 W/kg) in UHV (ultra-high voltage)/EHV (extra-high voltage) transmission networks [1–3]. This trend toward thinning poses significant challenges for cold rolling quality, which in turn places stringent demands on the service performance of work rolls in cold-rolling mills. Specifically, wear of these rolls can lead to strip shape deterioration, while surface defects on the rolls are readily replicated onto the steel strip surface, especially when rolling to such thin gauges. These replicated defects act as magnetic domain pinning sites, thereby increasing core loss [4,5]. Consequently, the microstructure and properties of roll materials, particularly wear resistance, directly determine the stability of the rolling process and the surface quality of silicon steel strips.

Check for updates

Received: 22 August 2026
Revised: 14 September 2026
Accepted: 18 September 2026
Published: 22 September 2026

Copyright: © 2026 by the authors. Licensee MDPI, Basel, Switzerland. This article is an open access article distributed under the terms and conditions of the Creative Commons Attribution (CC BY) license.

Cr12Mo1V1Co, a high-carbon high-chromium cold-work tool steel, is a promising candidate material for work rolls in silicon steel cold-rolling mills, primarily of the Sendzimir type. This alloy is derived from conventional D2 tool steel by the addition of approximately 0.3 wt.% cobalt. D2 steel possesses high hardness, excellent wear resistance, and good oxidation resistance at elevated temperatures, which, combined with its favorable hardenability, accounts for its widespread use in cold-working dies for operations such as stamping, heading, and extrusion [6–9]. However, its performance remains inadequate for the cold rolling of ultra-thin grain-oriented silicon steel strips.

To enhance the performance of D2 steel, considerable research efforts in recent years have focused on new processes related to the material itself and surface modifications. Research on the material itself has primarily explored advanced heat treatment routes. For example, dual austenitizing has been employed to inhibit excessive grain growth while enhancing hardness and toughness [10]. Cryogenic treatment has been applied to substantially reduce retained austenite content and promote the dispersion of secondary carbides, thereby improving wear resistance [11–14]. Alternatively, replacing the second stage for conventional graded quenching with bright quenching (KOH + NaOH salt bath quenching) can achieve a favorable balance between high hardness and toughness [15]. In essence, these heat treatment strategies are ultimately directed toward achieving precise control over the content, morphology, size, and distribution of key microstructural constituents [16–18]. In addition, surface modification of D2 steel has also been extensively investigated to improve its wear and corrosion resistance. Representative approaches include diffusion-based treatments such as gas and plasma nitriding [19], physical vapor deposition (PVD) of transition-metal nitride coatings (e.g., TiN, CrN, TiAlN), including multilayer and duplex architectures combining nitriding with coating deposition [20,21], and surface repair techniques such as overlaying welding and laser cladding with Co/Ni-based or high-entropy alloys [22,23].

Research on the wear behavior of die steels, represented by D2 steel, primarily focuses on their mechanisms and resistance. To investigate different wear mechanisms, such as adhesion, three-body abrasion, and two-body abrasion, methods including pin-on-disk tests, sand/rubber wheel apparatus tests, and reciprocating sliding tests are commonly employed [11,24–32]. Studies indicate that external factors influencing the wear rate include sliding speed, load, counterface material, lubrication condition and test environment (temperature, humidity, acidity/alkalinity). The effect of these factors varies significantly under different wear conditions and parameter ranges. For instance, Bourithis et al. [25] reported that in sand/rubber wheel tests, the wear rate of D2 steel increased with higher loads. In contrast, Ma et al. [24], using a similar setup, observed a decrease in wear rate with increasing load, attributing this to the fracture of abrasive particles under high loads, which reduces their cutting ability. In adhesive wear, the wear rate typically increases with sliding speed [33]. However, at speeds high enough to form a protective oxide layer, the wear rate may decrease [25]. The internal factors governing wear performance are predominantly the microstructural characteristics, such as the tempered martensite matrix, retained austenite, and carbides (including their content, size, shape and distribution). The influence of these microstructural features also differs under various wear conditions. For example, in three-body and two-body abrasion under relatively low loads, large carbides, due to their high hardness, can effectively resist abrasion and reduce wear [25]. Conversely, under high loads, the fracture and subsequent pull-out of these carbides can lead to a substantial increase in wear [33,34]. Generally, increased material hardness is beneficial for wear resistance. However, the associated reduction in toughness may cause localized spallation or fragmentation, ultimately increasing wear. Therefore, the tribological behavior of die steel is determined by a complex interplay between its microstructure

and the service environment. The experimental design should be tailored to its specific application scenarios.

When comprehensively considering service performance and production cost, Sendzimir mill work rolls made of Cr12Mo1V1Co steel are generally free from additional surface treatment, and their properties are determined by the final bulk heat treatment (quenching and tempering) process. Currently, relevant research on cobalt-containing D2 steel (i.e., Cr12Mo1V1Co steel) remains relatively scarce. Considering the sensitivity of die steel properties to quenching–tempering schedules, especially the complex effects of the combined action of multiple factors on material wear rate, this paper will systematically investigate the evolution behavior of microstructural constituents (including tempered martensite, carbides, and retained austenite) of Cr12Mo1V1Co steel under the condition of "high-temperature quenching plus high-temperature tempering". The relationship among heat treatment processes, microstructure, and mechanical properties will be established through hardness testing, impact toughness testing, and reciprocating friction and wear tests, with emphasis on analyzing the effects of various microstructural factors on the wear resistance of the material. The findings of this study are anticipated to provide a theoretical basis for optimizing the heat treatment process of Cr12Mo1V1Co steel for work roll applications.

2. Materials and Methods

The chemical compositions of Cr12Mo1V1Co (Xinyuan Roller Industry Company Limited, Yixing, China) in this study are listed in Table 1. The equilibrium phases and their compositions of this alloy under constant pressure were calculated using JmatPro (Version 7.0) thermodynamic software in the temperature range of 400–1600 °C with a step size of 10 °C. The calculation was conducted based on the principle of minimizing Gibbs free energy, utilizing the iron-based database integrated in the software. The effect of temperature on the precipitation amount of each phase was output and analyzed.

Table 1. The chemical compositions of Cr12Mo1V1Co (wt%).

C	Si	Mn	Cr	Mo	Co	V	Al	Ti	Fe
1.66	0.45	0.36	11.75	0.86	0.29	1.13	0.031	0.024	Bal.

Rectangular samples with the size of 6 mm × 12 mm × 12 mm were cut from 1/2 radius position of a wrought bar with a diameter of 88 mm, which was spheroidizing annealed. The original microstructure consists of spheroidal carbides (<2 μm in diameter), irregularly shaped eutectic carbides, and ferrite matrix (Figure 1).

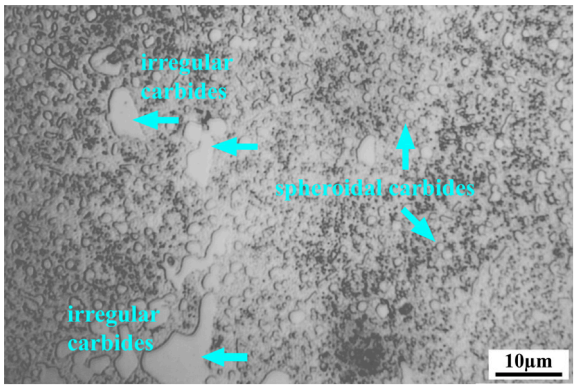


Figure 1. Microstructure of Cr12Mo1V1Co steel in the spheroidization-annealed state.

Heat treatment was performed using a KSL-1400X box-type resistance furnace (Hefei Kejing Materials Technology Co., Ltd., Hefei, China). The Cr12Mo1V1Co steel samples were austenitized at 1040 °C, 1060 °C, 1080 °C, 1100 °C, and 1120 °C for 30 min, followed by oil quenching to approximately 100 °C. To prevent cracking, the quenched samples were immediately triple-tempered at 480 °C, 500 °C, and 520 °C, respectively, with each tempering cycle lasting 4 h followed by air cooling.

The spheroidizing annealed, quenched, and tempered samples were mechanically ground and polished, followed by etching in a solution of 1 g $FeCl_3$ + 3 mL HCl + 12 mL H_2O. The microstructure was analyzed using an OLYMPUS metallurgical microscope(Olympus Corporation, Hachioji, Tokyo, Japan). The fine morphology of carbides and martensite was examined using a JSM-6360LV scanning electron microscope (SEM) (JEOL Ltd., Mitaka, Tokyo, Japan) equipped with a GENESIS 2000XM60 energy-dispersive spectrometer (EDS) (EDAX Inc., Mahwah, NJ, USA). Carbide volume fractions were quantified by image analysis of micrographs taken at 200× magnification. For each specimen, five randomly selected fields of view were analyzed (single field ≈ 0.12 mm^2; total analyzed area ≈ 0.6 mm^2 per specimen). Carbides were isolated from the matrix using grayscale thresholding in Adobe Photoshop (Version, 2024), with the threshold level kept constant across all fields of the same specimen; particle boundaries were manually verified and corrected where necessary. The results were cross-validated using ImageJ software(Version, 1.53h) to confirm the reliability of the procedure. Carbide particles were classified into different categories based on their size and aspect ratio.

Phase analysis of carbides and matrix was conducted using an Ultima-IV X-ray diffractometer (Rigaku Corporation, Akishima, Tokyo, Japan), with a scanning angle ranging from 30 ° to 100 °. Scanning rates of 10 °/min and 2 °/min were employed for qualitative and quantitative analysis, respectively. The volume fraction of retained austenite (γ phase) was quantified according to the Chinese standard YB/T 5338-2019 using the five-line six-pair method ((200) and (211) in a phase, (200), (220), and (311) in γ phase). The reported value is the arithmetic mean of the six peak pairs. According to the precision specification of the standard, the relative standard deviation of this method is within 2% for γ-phase contents above 20 vol.% and within 3% for contents of 10–20 vol.%.

The Rockwell hardness of the quenched and tempered specimens was measured following GB/T 230.1-2018. An average value was calculated from five indentations per specimen. Charpy impact testing of all tempered samples was carried out at ambient temperature employing unnotched rectangular bars (10 mm × 10 mm × 55 mm), according to GB/T 229-2020. For each heat-treatment regime, three replicate specimens were tested, and the average absorbed impact energy was presented. Additionally, the fracture surfaces of the impacted specimens were examined to analyze the fracture morphology.

Dry sliding wear tests were conducted on a multi-functional tribometer (Rtec, MFT-3000) (Rtec Instruments, San Jose, CA, USA) for all tempered samples. A reciprocating ball-on-disk configuration was employed, using an upper Si_3N_4 ceramic ball (12.7 mm in diameter, 1700 HV, surface roughness Ra ≈ 0.02 μm) as the counterface (Figure 2). Prior to wear testing, all specimens were mechanically ground and polished (final polishing with 2.5 μm diamond paste), yielding an initial surface roughness of Ra ≈ 0.05 μm. The tests were performed at a normal load of 100 N, sliding speed of 0.02 m/s, stroke length of 0.003 m, and duration of 30 min, giving a total sliding distance of 36 m (0.02 m/s × 1800 s). The wear scar profile and wear volume were measured and analyzed using a Rtec UP-3000 three-dimensional optical profiler (Rtec Instruments, San Jose, CA, USA). The volumetric wear rate (Wr) was calculated using the following formula:

$$W_r = \frac{V}{(F \cdot s)} \quad (1)$$

where V represents the wear volume (mm^3), F denotes the applied load (N), and s stands for the sliding distance (m). Three independent wear tests were performed for each heat-treatment condition, and average values were adopted for further analysis. The morphology and characteristics of the wear scars were examined using a ZEISS MERLIN compact field emission scanning electron microscope (FE-SEM) (Carl Zeiss Microscopy GmbH, Oberkochen, Germany).

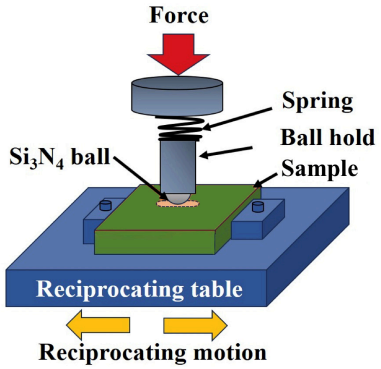


Figure 2. Schematic of the reciprocating sliding friction at room temperature.

Standard deviations derived from repeated measurements of hardness, absorbed impact energy and volumetric wear rate are reported as error bars in the corresponding result figures.

3. Results

3.1. Microstructural Characterization

3.1.1. Calculation and Identification of Precipitated Phases

Figure 3a illustrates the equilibrium phase constitution of Cr12Mo1V1Co steel, which serves as a thermodynamic baseline for the candidate phases and their stability temperature ranges. It can be seen that under solid-state conditions, the material is mainly composed of austenite, ferrite, and three types of carbides: M_7C_3, MC, and $M_{23}C_6$. The dominant metallic elements in the carbides are as follows: Cr and Fe in M_7C_3; V in MC; and Cr, Fe, and Mo in $M_{23}C_6$. Table 2 lists the temperature ranges for the stability of each phase. Figure 3b presents the mass fraction of cobalt (Co) in individual phases at different temperatures. As an alloying element in the modified D2 steel, Co is predominantly dissolved in the matrix, with small amounts present in the carbides.

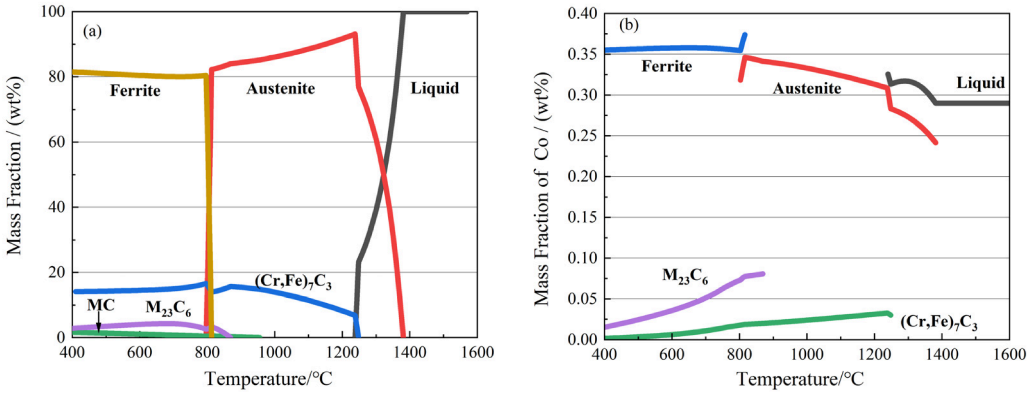


Figure 3. Thermodynamic calculation results of Cr12Mo1V1Co steel: (**a**) mass fraction of precipitated phases; (**b**) mass fraction of Co in different phases.

Table 2. Calculated temperature ranges of phase stability in Cr12Mo1V1Co steel (°C).

Liquid	Austenite	Ferrite	M_7C_3	$M_{23}C_6$	MC
1237.7~	796.3~1380.8	~812.7	~1248.5	~869.2	~955.3

Figure 4 shows the X-ray diffraction (XRD) patterns of Cr12Mo1V1Co steel samples under various heat treatment conditions. In all the patterns of as-quenched samples, a body-centered cubic phase (i.e., martensite) and carbide $(Cr,Fe)_7C_3$ are detected (Figure 4a). It should be noted that the crystal structure of martensite is body-centered tetragonal, representing a supersaturated solid solution of carbon in iron. However, it is indexed as ferrite because the resolution of the diffractometer is insufficient to resolve the tetragonality of the martensite [28]. When the quenching temperature is 1100 °C, the peaks of retained austenite (R_A) appear in the XRD patterns (γ in Figure 4a). These peaks become increasingly pronounced in the sample quenched at 1120 °C. This can be attributed to the extensive dissolution of alloying elements from the carbides into the matrix at elevated quenching temperatures, which enhances the stability of austenite and lowers the martensite transformation temperature, consequently leading to the retention of austenite after oil quenching. Quantitative measurements indicate that the volume fraction of R_A is approximately 20.1% and 44.4% at quenching temperatures of 1100 °C and 1120 °C, respectively. It should be noted that during low-temperature quenching (1040–1080 °C), the retained austenite cannot be detected because its fraction is below the detection threshold of the X-ray diffractometer.

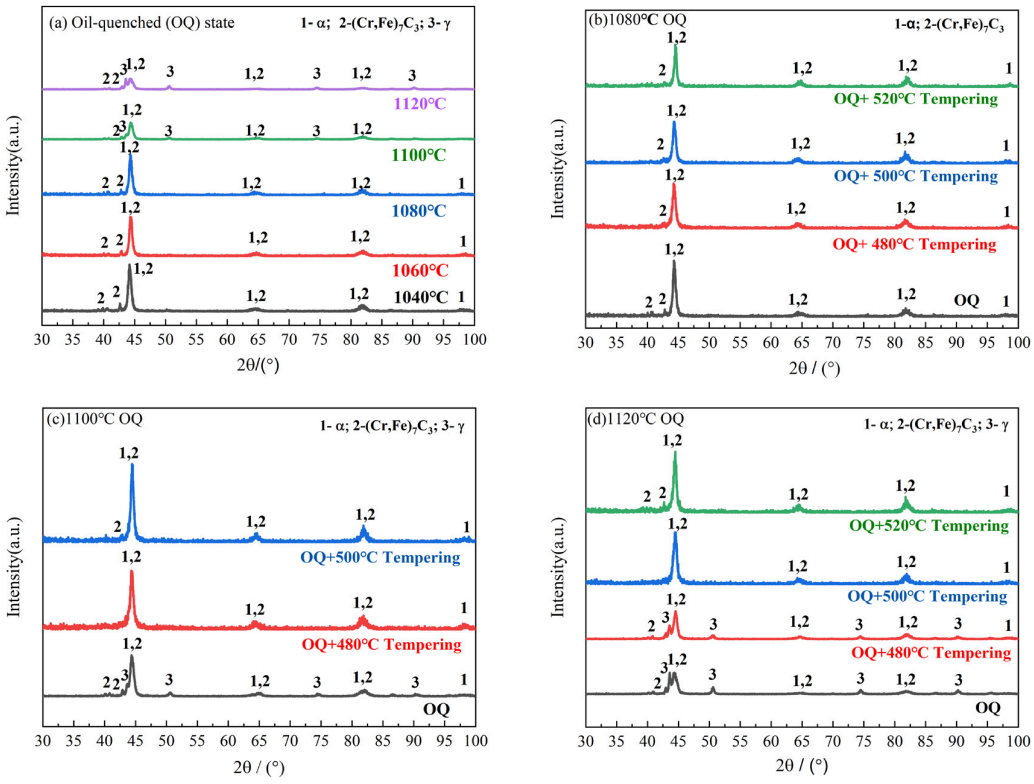


Figure 4. XRD patterns of differentially heat-treated samples: (**a**) as-quenched state; (**b**) 1080 °C quenched + tempering; (**c**) 1100 °C quenched + tempering; (**d**) 1120 °C quenched + tempering.

The phase assemblage remains stable after tempering for samples quenched at 1040–1080 °C, as exemplified by the 1080 °C samples (Figure 4b). In contrast, for samples quenched at 1100 °C, the R_A peaks disappear after tempering (Figure 4c), indicating that it has decomposed to a volume fraction below the detection limit of the equipment. When the quenching temperature is 1120 °C, distinct R_A peaks persist in the XRD patterns af-

ter triple tempering at 480 °C, with a corresponding volume fraction of approximately 11.5% as determined by quantitative analysis. These peaks disappear when the tempering temperature is increased to 500 °C and 520 °C (Figure 4d). Studies indicate that during high-temperature tempering, the principal alloying elements in the retained austenite precipitate as carbides. This precipitation reduces the stability of the austenite, causing it to transform into martensite during subsequent cooling after tempering—a phenomenon known as secondary quenching [13,35]. XRD results reveal that samples quenched at higher temperatures require a correspondingly higher tempering temperature to achieve complete decomposition of the retained austenite.

3.1.2. Microstructural Morphology

Typical microstructural morphologies of Cr12Mo1V1Co steel in the oil-quenched state are shown in Figure 5. The quenched sample is composed of plate martensite, irregular carbides, and fine spherical carbides. Retained austenite detected by XRD cannot be distinguished in either optical micrographs or SEM images. The maximum size of martensite plates is approximately 10.5 μm in the 1040 °C-quenched sample. The lengths of the irregular carbides exceed 25 μm, while the diameter of the spheroidal carbides is around 1.5 μm. Quenching temperature has little effect on the size of martensite plates, but exerts a significant influence on carbides. When the quenching temperature reaches 1080 °C, the dissolution traces at the edges of large irregular carbides are significantly intensified, and the local fragmentation at carbide edges is aggravated, forming fragments smaller than 5 μm (Figure 5b,c). Quantitative metallographic analysis shows that the volume fraction of carbide fragments increases from 1.2% for the sample quenched at 1040 °C to 2.5% for that quenched at 1120 °C. Correspondingly, the volume fraction of intact irregular carbides decreases from 6.3% to 3.1% (Table 3). On the other hand, the spheroidal carbides dissolve extensively with increasing quenching temperature. When the quenching temperature increases to 1100 °C and 1120 °C, the proportion of spheroidal carbides drops sharply to 0.4% and 0.3%, respectively.

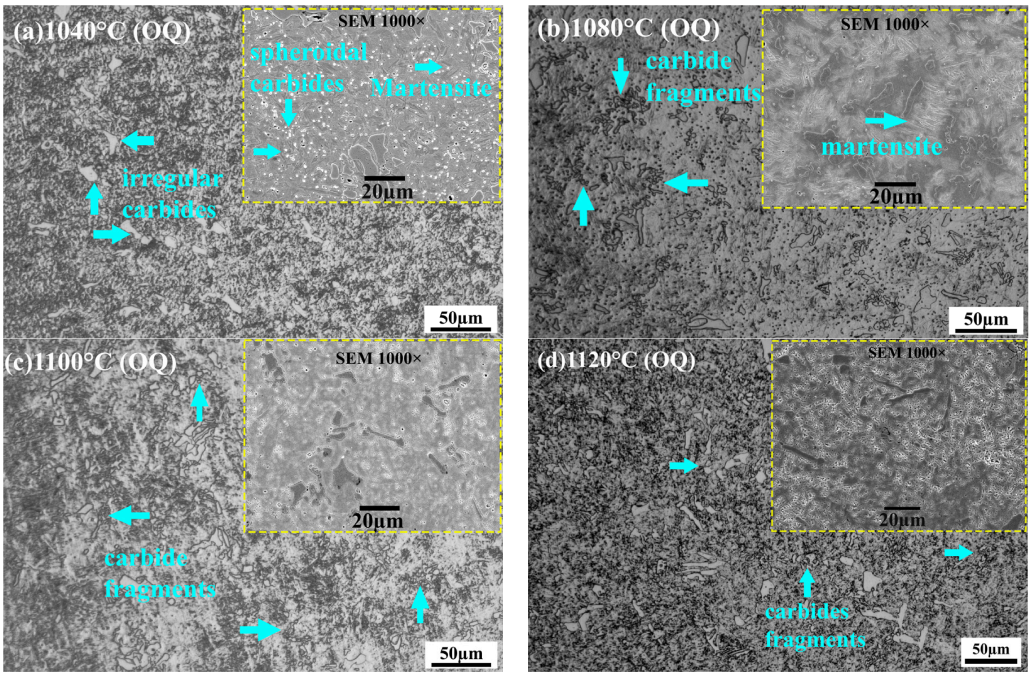


Figure 5. Microstructures and corresponding magnified images of as-quenched samples: (**a**) 1040 °C; (**b**) 1080 °C; (**c**) 1100 °C; (**d**) 1120 °C.

Table 3. Volume fraction of carbides with different shapes (%).

	1040 °C				**1060 °C**				**1080 °C**			
	OQ	**Tempered**			**OQ**	**Tempered**			**OQ**	**Tempered**		
		480 °C	**500 °C**	**520 °C**		**480 °C**	**500 °C**	**520 °C**		**480 °C**	**500 °C**	**520 °C**
unfragmented irregular carbides	6.3 ± 0.6	6.2 ± 0.6	6.0 ± 0.4	6.1 ± 0.3	6.7 ± 0.5	7.0 ± 0.4	6.8 ± 0.3	6.2 ± 0.6	5.4 ± 0.7	5.8 ± 0.3	5.5 ± 0.7	5.6 ± 0.6
carbide fragments	1.2 ± 0.2	1.3 ± 0.3	1.4 ± 0.2	1.6 ± 0.1	1.0 ± 0.3	1.6 ± 0.2	1.5 ± 0.3	1.6 ± 0.2	1.6 ± 0.3	2.0 ± 0.1	1.3 ± 0.3	1.3 ± 0.3
irregular carbides (unfragmented+ fragmented)	7.5 ± 0.6	7.5 ± 0.7	7.4 ± 0.4	7.7 ± 0.3	7.7 ± 0.6	8.6 ± 0.4	8.3 ± 0.4	7.8 ± 0.6	7.0 ± 0.8	7.8 ± 0.3	6.8 ± 0.8	6.9 ± 0.7
spheroidal carbides	2.1 ± 0.4	4.4 ± 0.6	3.8 ± 0.3	4.0 ± 0.4	1.9 ± 0.3	3.8 ± 0.6	3.5 ± 0.6	4.0 ± 0.4	1.6 ± 0.3	3.5 ± 0.4	2.3 ± 0.2	2.5 ± 0.3

	1100 °C				1120 °C			
	OQ	tempered			OQ	tempered		
		480 °C	500 °C	520 °C		480 °C	500 °C	520 °C
unfragmented irregular carbides	3.4 ± 0.4	4.2 ± 0.3	3.7 ± 0.4	5.0 ± 0.3	3.1 ± 0.3	3.9 ± 0.5	3.4 ± 0.4	4.0 ± 0.3
carbide fragments	2.3 ± 0.4	2.1 ± 0.3	1.8 ± 0.5	2.2 ± 0.3	2.5 ± 0.3	2.4 ± 0.4	2.4 ± 0.4	2.7 ± 0.5
irregular carbides (unfragmented+ fragmented)	5.7 ± 0.6	6.3 ± 0.4	5.5 ± 0.6	7.2 ± 0.4	5.6 ± 0.4	6.3 ± 0.6	5.8 ± 0.6	6.7 ± 0.6
spheroidal carbides	0.4 ± 0.2	0.6 ± 0.2	0.5 ± 0.1	0.7 ± 0.1	0.3 ± 0.2	0.6 ± 0.1	0.6 ± 0.2	0.6 ± 0.1

https://doi.org/10.3390/met16101055

After three cycles of tempering at different temperatures, the matrix of samples still exhibited acicular martensite morphology (magnified images in Figure 6(a2–d2)), i.e., tempered martensite microstructure. The size of tempered martensite plates is reduced compared with the as-quenched state, with a typical length of approximately 6.5 μm. The tempering process showed minimal impact on both the content of irregular carbides and their fragmentation behavior (Table 3). In contrast, the proportion of spheroidal carbides in tempered specimens typically doubled compared to their as-quenched counterparts, indicating that the secondary carbides formed during tempering are spheroidal. For instance, in samples quenched at 1040 °C followed by tempering, the spheroidal carbide fraction increased from 2.1% to approximately 4% (Figure 5a vs. Figure 6(a1–a3) and Table 3). For the 1100 °C- and 1120 °C-quenched sample series, the proportion of spheroidal carbides consistently remained below 1% after tempering, although a significant increase was observed compared to the as-quenched state. Quantitative analysis shows that tempering temperature has little effect on the volume fractions of spheroidal carbides at the same quenching temperature, but their size is significantly coarsened when tempered at 520 °C (Figure 6(a3–d3)).

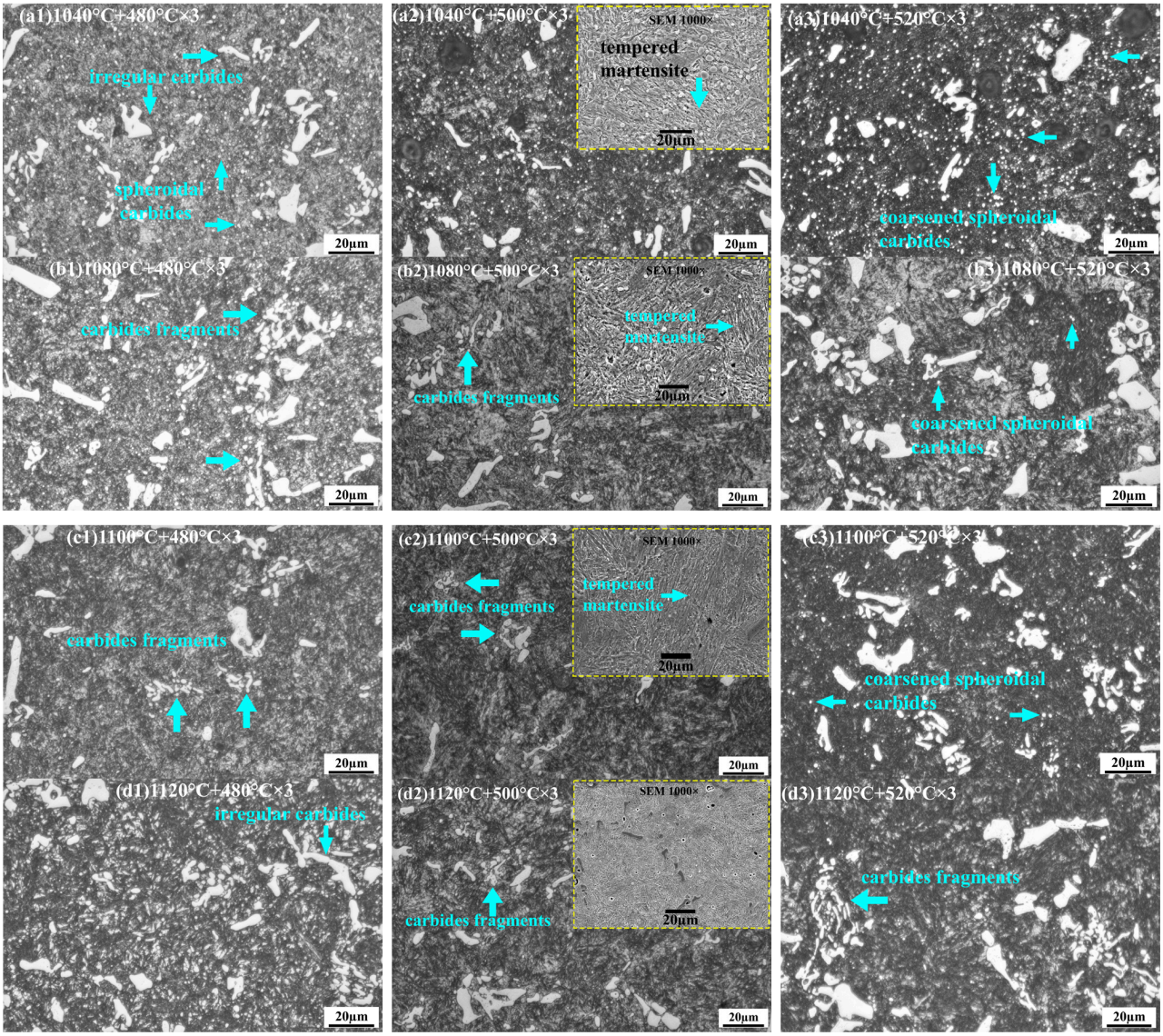


Figure 6. Microstructures and corresponding magnified images of samples under different heat treatment conditions: (**a1–a3**) 1040 °C quenching series; (**b1–b3**) 1080 °C quenching series; (**c1–c3**) 1100 °C quenching series; (**d1–d3**) 1120 °C quenching series.

The chemical compositions of irregular and spheroidal carbides were determined by EDS; for each type of carbide, at least five particles were measured on randomly selected locations, and the average compositions are listed in Table 4. Consistent with tempered D2 steel, these precipitates are rich in Cr and Fe, with appreciable amounts of Mo and V. While the identification of such carbides in D2 steel remains controversial in the literature, being reported as either M_7C_3 [25,28] or $M_{23}C_6$ [13,36,37], the present results support an M_7C_3-type identification for both the irregular and spheroidal carbides on the basis of two lines of evidence: Distinct $(Cr,Fe)_7C_3$ reflections are present in the XRD patterns of both as-quenched and tempered specimens, whereas no characteristic reflections of $M_{23}C_6$ or MC carbides are discernible—considering that the total carbide content exceeds 8 vol. % (Table 3), well above the detection limit of the present XRD method, such carbides would have been detected if they were predominantly $M_{23}C_6$ or MC. EDS analysis reveals that the V content in both carbide types remains low, incompatible with the stoichiometry of V-rich MC carbides and instead consistent with that of M_7C_3.

Table 4. Average chemical compositions of carbides in Cr12Mo1V1Co steel determined by EDS (wt%).

	C	Cr	V	Mo	Fe
irregular carbides	10.1	42.7	5.6	5.0	36.7
spheroidal carbides	12.0	38.9	4.1	2.9	42.2

3.2. Room Temperature Hardness

Figure 7 presents the room-temperature hardness of Cr12Mo1V1Co steel samples under different heat treatment conditions. It can be observed that the as-quenched specimens exhibit hardness values ranging between 56–62 HRC, with a decreasing trend as the quenching temperature increases. The reduced hardness can be ascribed to the appearance of soft retained austenite, especially at 1100 °C and 1120 °C. In addition, an elevated quenching temperature promotes considerable dissolution of carbides, which further contributes to the hardness reduction of the as-quenched specimens. The effect of tempering on hardness depends strongly on the prior quenching temperature. For specimens quenched at 1040–1080 °C, tempering leads to a decrease in hardness. The hardness values after tempering at 480 °C and 500 °C are comparable, while a much more pronounced reduction occurs upon tempering at 520 °C. The softening effect during tempering arises from the decomposition of martensite into tempered martensite. This originates from weakened solid-solution strengthening owing to reduced carbon supersaturation, together with the diminished dislocation strengthening and twin boundary strengthening [38]. The finely dispersed spheroidal carbides precipitated during tempering (Figure 6) afford a certain strengthening effect, thereby mitigating tempering softening. However, coarsening of these carbides significantly weakens their strengthening contribution, resulting in a further decrease in tempering hardness, as seen in the 520 °C-tempered samples. For the samples quenched at 1100 °C, the hardening effects during tempering, including the transformation of retained austenite into martensite (secondary quenching) and the fine precipitation of carbides, are essentially balanced with the softening effect caused by martensite decomposition. Consequently, the hardness remains stable at 58–60.5 HRC. For the samples quenched at 1120 °C, approximately 11.5 vol. % retained austenite persisted after tempering at 480 °C; hence, the hardness increased only slightly relative to the as-quenched state. After tempering at 500 °C, the retained austenite is almost eliminated, and the room-temperature hardness increases to 62.5 HRC. For the samples quenched at both 1100 °C and 1120 °C, a decline in hardness is observed after tempering at 520 °C.

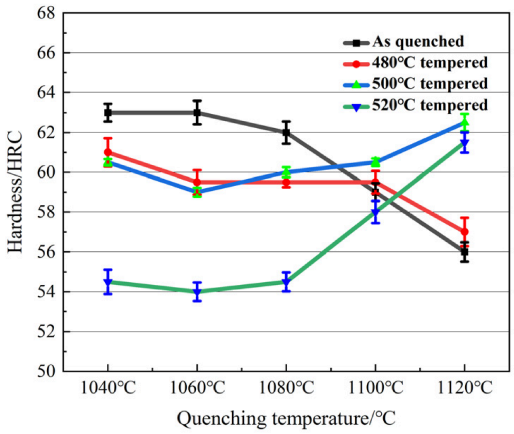


Figure 7. Room-temperature hardness of Cr12Mo1V1Co steel in different states.

3.3. Impact Toughness

Figure 8 illustrates the impact absorbed energy of the tempered specimens under various heat treatment regimes. For samples quenched at 1040–1080 °C, the impact absorbed energy of unnotched specimens shows an approximately inverse trend with hardness; those tempered at 520 °C display the lowest hardness and the highest impact toughness. The impact absorbed energy of the tempered specimens quenched at 1100 °C and 1120 °C is lower than that of their counterparts quenched at 1040–1080 °C, and the influence of tempering temperature on impact toughness is also less pronounced for these specimens than for those quenched at 1040–1080 °C. Among the 1100 °C- and 1120 °C-quenched specimens, the batches tempered at 480 °C and 500 °C respectively exhibit relatively high impact toughness.

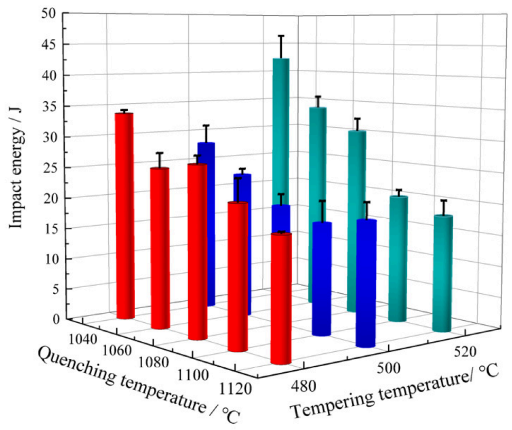


Figure 8. Impact absorbed energy of samples under different heat treatment conditions. Red, blue, and cyan bars represent the samples tempered at 480 °C, 500 °C, and 520 °C, respectively.

Figure 9 shows the typical impact fracture morphologies of samples under different quenching and tempering treatments (magnified views in dashed boxes), covering samples with different impact absorbed energy. It can be seen that the fracture surfaces of all samples present abundant dimples along with tear ridges, exhibiting ductile fracture characteristics. Local quasi-cleavage facets are observed on the fracture surfaces. These regions are relatively flat without obvious plastic deformation, and cracks are found in some of them. The observed flat regions exhibit dimensions and morphologies consistent with the presence of large irregular carbides (Figure 6), suggesting an intrinsic relationship. It is reported that the interfacial bonding strength between carbide and matrix is lower than the cohesive strength of the matrix itself [34]. When impact cracks propagate to the carbide/matrix

interface, they preferentially extend rapidly along the interface, leading to carbide detachment and forming flat quasi-cleavage facets that match the size of the carbides, which always exerts an adverse effect on the impact toughness of the steel [39]. However, further observation shows that samples with relatively low impact toughness do not exhibit more quasi-cleavage facets. On the contrary, although the 1040–1080 °C-quenched sample series exhibit a larger volume fraction of irregular carbides (Table 3), which can promote the formation of quasi-cleavage facets, their impact toughness is relatively higher.

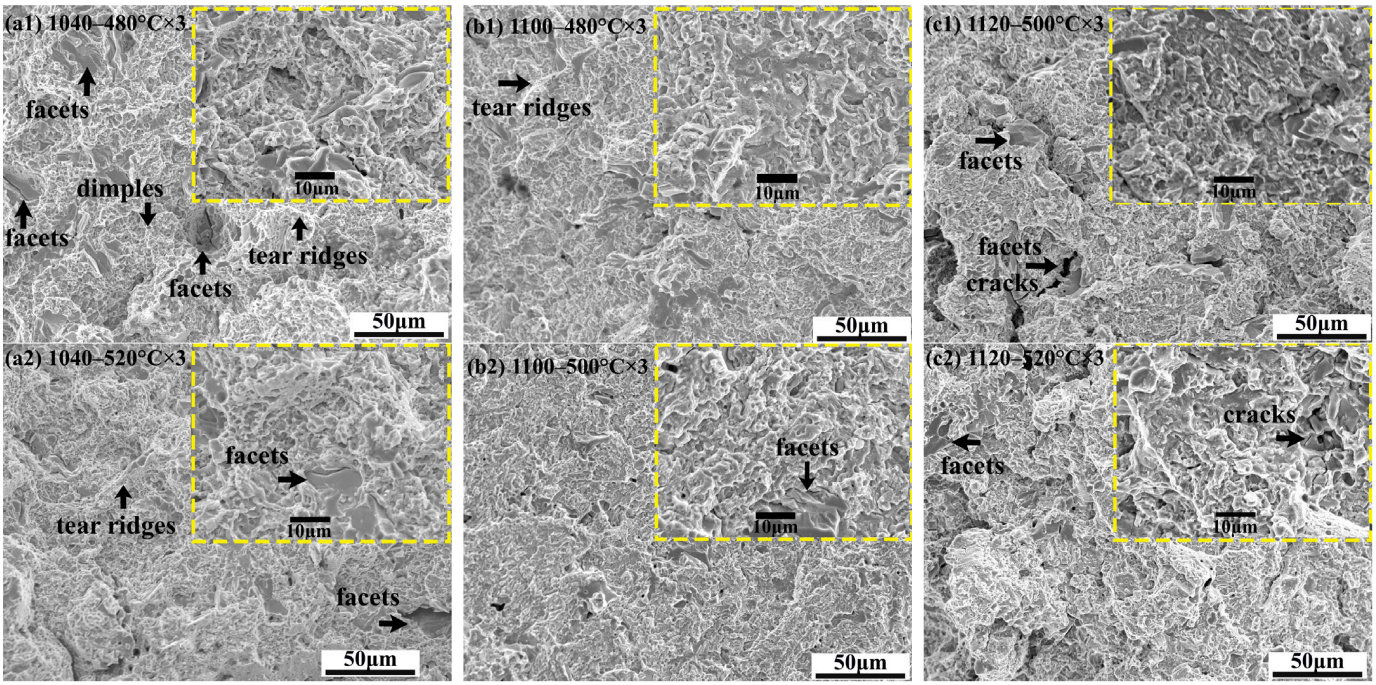


Figure 9. Impact fracture morphologies and magnified images of samples under different heat treatment: (**a1**,**a2**) quenched at 1040 °C + tempered at 480 °C/520 °C; (**b1**,**b2**) quenched at 1100 °C + tempered at 480 °C/500 °C; (**c1**,**c2**) quenched at 1120 °C + tempered at 500 °C/520 °C.

From the fracture morphology, samples with higher impact absorbed energy have deeper and finer dimples on the fracture surfaces. For the 1040–1080 °C-quenched sample series, martensite decomposition becomes more sufficient with increasing tempering temperature. Consequently, the matrix exhibits substantially improved plastic deformation capacity. Upon impact, the matrix dissipates energy through enhanced plastic flow, which results in numerous deep and uniformly sized dimples on the fracture surface. In contrast, for the 1100–1120 °C-quenched samples, the combination of secondary quenching during tempering and enhanced tempering stability (due to massive alloying element re-dissolution at high quenching temperatures) results in less complete martensite decomposition compared with the 1040–1080 °C-quenched samples at the same tempering temperature. Consequently, the matrix exhibits limited plastic deformation capacity during impact, producing generally shallow dimples on the fracture surfaces.

3.4. Friction and Wear Tests

3.4.1. Wear Rate and Friction Coefficient

Figure 10 presents the volumetric wear rates of Cr12Mo1V1Co steel subjected to various quenching and tempering treatments. The wear rates range from 1.30×10^{-6} to 6.39×10^{-6} $mm^3/(N \cdot m)$. For samples quenched at 1040 °C, 1060 °C, and 1080 °C, tempering temperature exerts a comparable influence on wear rate: samples tempered at 480 °C and 500 °C exhibit similar wear rates, whereas increasing the tempering temperature to

520 °C leads to a substantial increase (approximately two-fold). At a quenching temperature of 1100 °C, the wear rate increases monotonically with increasing tempering temperature. In contrast, the 1120 °C-quenched samples show a minimum wear rate at 500 °C, with higher rates obtained at both lower and higher tempering temperatures. Overall, samples quenched at 1040–1060 °C deliver comparable wear rates under identical tempering conditions. Raising the quenching temperature to 1080 °C produces a modest reduction in wear rate. Further increasing the quenching temperature to 1100 °C and 1120 °C gives rise to a more distinct reduction in wear rate after tempering.

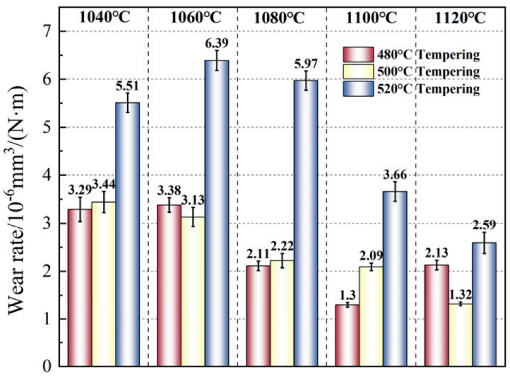


Figure 10. Wear rates of samples subjected to different heat treatment conditions.

Typical curves illustrating the relationship between friction coefficient and sliding time are shown in Figure 11a (1100 °C quenching series). The friction process exhibits two distinct stages: running-in and steady-state. The running-in stage primarily involves mutual accommodation between the Cr12Mo1V1Co steel and the counterface ball at the onset of friction, characterized by considerable fluctuation in the friction coefficient. The duration of this stage varies slightly with heat treatment conditions, remaining approximately 400 s. Under various heat treatment conditions, the friction coefficient stabilizes within the range of 0.59–0.68 during steady-state wear (Figure 11b).

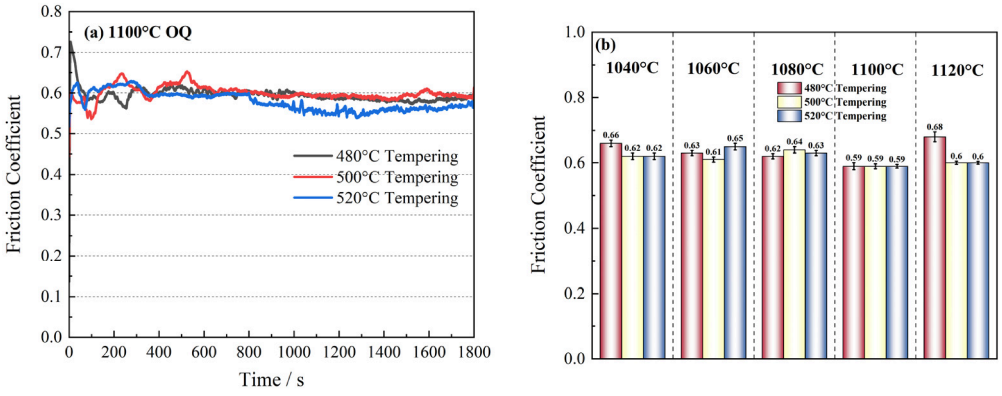


Figure 11. Friction behavior of samples under different heat treatment conditions: (**a**) friction coefficient versus sliding time for the 1100 °C quenching series, (**b**) steady-state friction coefficients.

3.4.2. Wear Morphology

Typical worn surface morphologies of samples with distinct wear rate ranges are presented in Figures 12–14. Figure 12 illustrates the wear scar characteristics of the sample quenched at 1100 °C and tempered at 480 °C (representative of samples with wear rates below 2.0×10^{-6} mm^3/(N·m)). The entire wear region exhibits extensive parallel plowing grooves, with deeper grooves at the center of the wear scar and shallower ones at the periphery (Figure 12a). The cross-sectional profile along line A-A′ displays numerous

steep fluctuations, consistent with the groove morphology, with a maximum wear depth of approximately 7.7 μm (Figure 12b). Combined SEM and EDS analyses reveal that the wear region comprises oxide and substrate zones (Table 5). The oxide zone exhibits elevated Si content, suggesting that debris from the Si_3N_4 counterface ball also undergoes oxidation. Spallation of the oxide layer is observed, with the exposed regions exhibiting irregular topography. Cracks penetrating both the oxide layer and the substrate are also present and are oriented perpendicular to the plowing direction. Additionally, large irregular carbides exhibit incipient detachment from the matrix, with localized fragmentation and subsequent small-scale pull-out (Figure 12d,e).

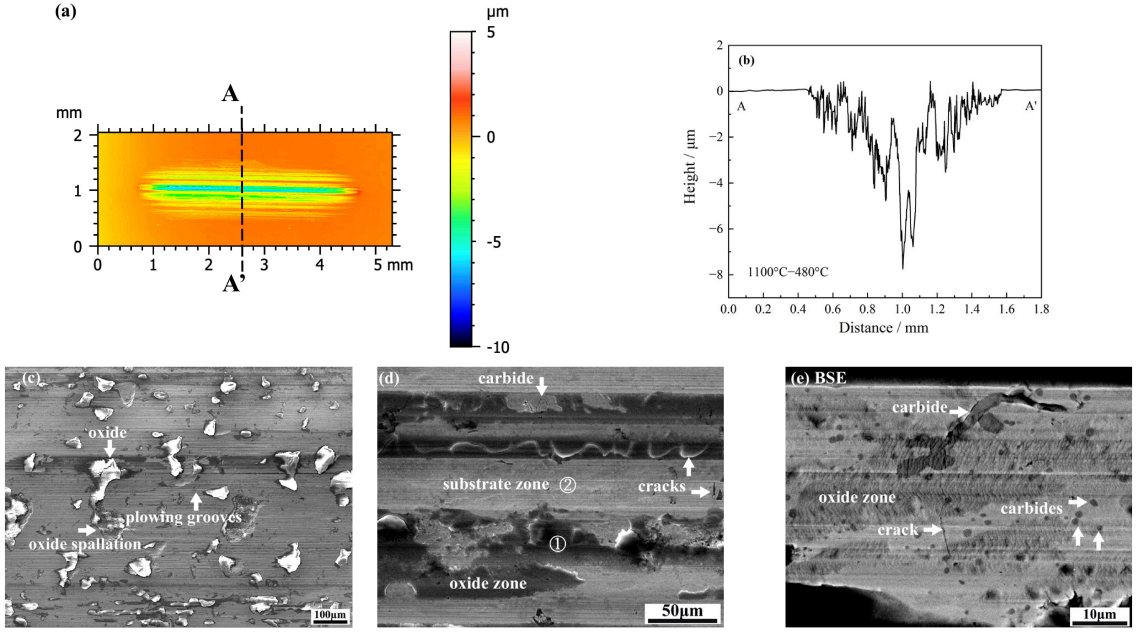


Figure 12. Wear morphologies of the sample quenched at 1100 °C and tempered at 480 °C: (**a**) wear track depth contour map; (**b**) cross-sectional profile along line A–A′; (**c**–**e**) surface morphologies of the wear scar.

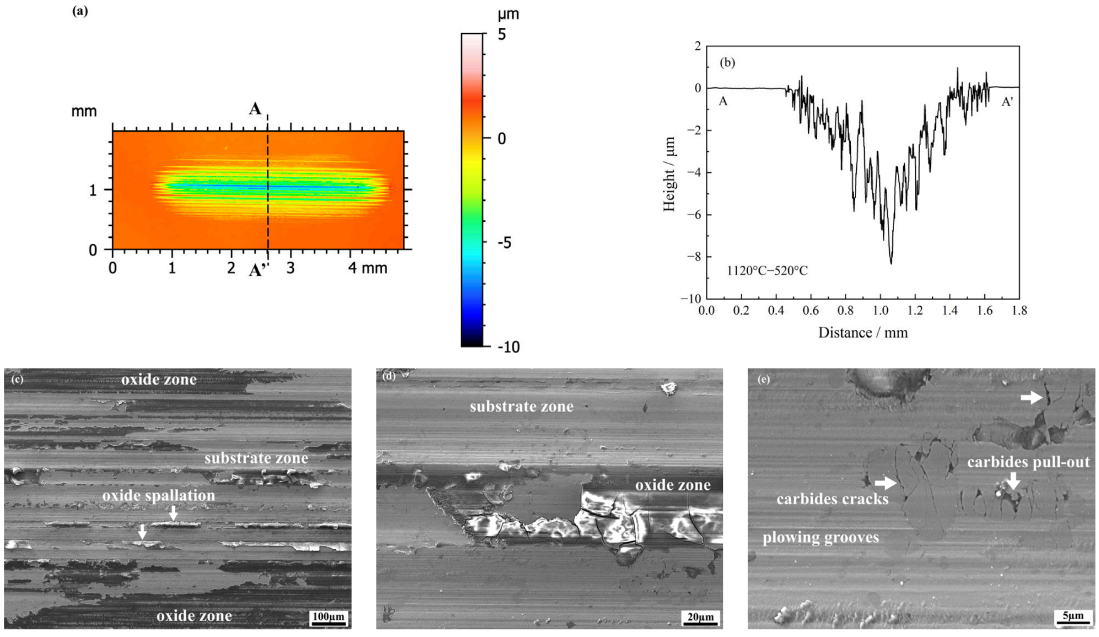


Figure 13. Wear morphologies of the sample quenched at 1120 °C and tempered at 520 °C: (**a**) wear track depth contour map; (**b**) cross-sectional profile along line A–A′; (**c**–**e**) surface morphologies of the wear scar.

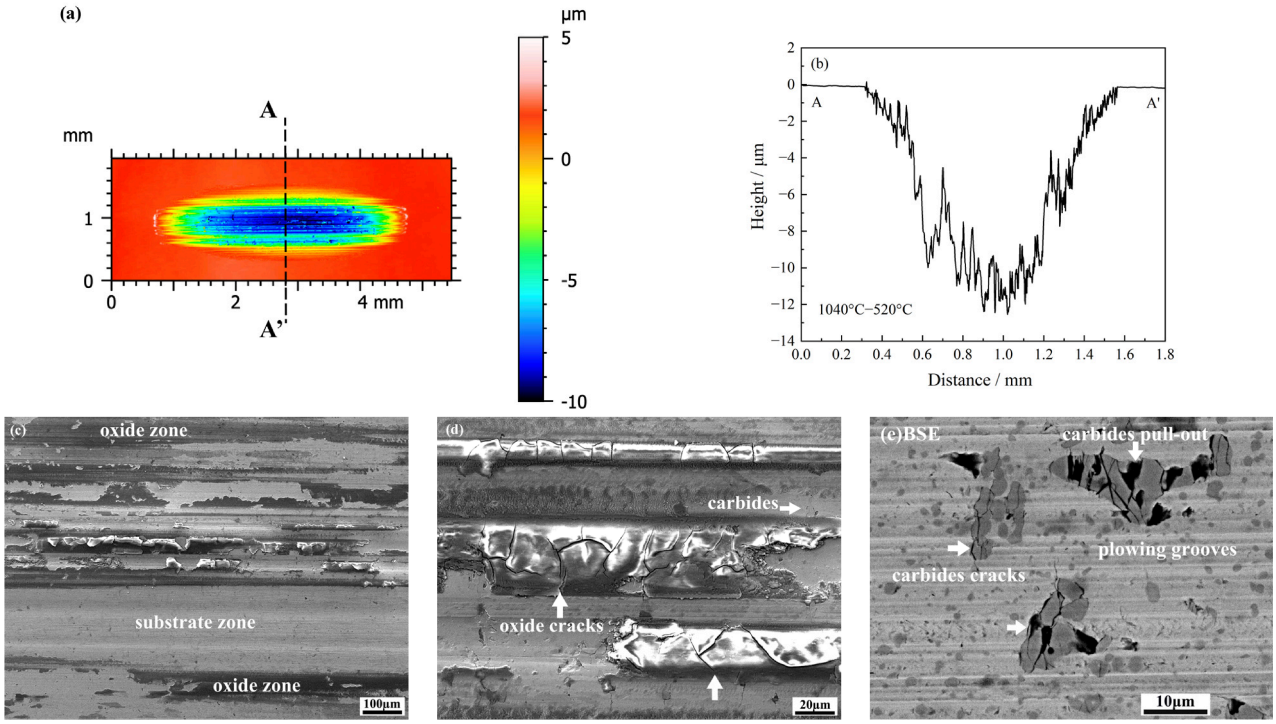


Figure 14. Wear morphologies of the sample quenched at 1040 °C and tempered at 520 °C: (**a**) wear track depth contour map; (**b**) cross-sectional profile along line A–A′; (**c**–**e**) surface morphologies of the wear scar.

Table 5. Chemical compositions of different regions on the worn surface (wt%).

Position	O	Si	Mo	V	Cr	Fe	Co
①	7.9	18.1	1.4	1.7	15.9	54.3	0.6
②	-	0.7	1.0	0.6	9.5	87.5	0.7

The wear morphology of the sample quenched at 1120 °C and tempered at 520 °C is shown in Figure 13. This specimen is representative of samples with wear rates of 2.0–3.0 × 10^{-6} $mm^3/(N{\cdot}m)$. The worn region still consists of oxide and substrate zones, with parallel plowing grooves running across both zones. Compared with the 1100–480 °C specimen, the 1120–520 °C sample shows an overall greater wear depth, especially at the center of the wear scar (Figure 13a,b). Additionally, the fraction of the oxide zone rises, and cracks within large oxide agglomerates become more prominent. Cracks and carbide pull-out of large carbides are also evident (Figure 13d). Samples with wear rates of 3.0–4.0 × 10^{-6} $mm^3/(N{\cdot}m)$ display comparable wear-morphology features. The plowing grooves become even deeper, with pronounced deepening particularly at the edges of the wear scar.

Figure 14 presents the wear morphology of the sample subjected to 1040 °C quenching and 520 °C tempering, representing samples with wear rates exceeding 5.0 × 10^{-6} $mm^3/(N{\cdot}m)$. The wear region exhibits substantial enlargement in both depth and width, with the maximum wear depth reaching 12.5 μm along section A–A′. The wear characteristics remain consistent with those of the previously described samples, but the proportion of cracked oxide increases further. Additionally, fracture and pull-out of large carbides become more severe (Figure 14e), corresponding to the scattered deep blue spots observed in Figure 14a.

4. Discussion

4.1. Wear Mechanisms

The worn surface morphology of Cr12Mo1V1Co steel is primarily characterized by parallel grooves, oxide layers (with partial spallation), and cracks perpendicular to the grooves. Although detached debris from the counterpart was observed adhering to the sample surface, typical signatures of severe adhesive wear, such as material smearing or extensive adhesive transfer, were absent. Therefore, based on the present experimental conditions, the dominant wear mechanisms are identified as abrasive wear, oxidative wear, and fatigue wear, with adhesive wear being negligible [11,26,33,40]. The wear behavior of Cr12Mo1V1Co steel proceeds through distinct material removal stages. Initial surface damage occurs via two-body abrasion, in which the harder Si_3N_4 counterface and its asperities directly plow the steel substrate and produce parallel grooves. This mechanism evolves into three-body abrasion once wear debris, consisting of metallic fragments, detached carbide particles, and counterpart debris, enters the contact interface. Simultaneously, frictional heating promotes surface oxidation. As abrasives plow across the surface, material is displaced towards both sides. Under reciprocating motion, such displacement induces stresses oriented perpendicular to the plowing direction, which eventually nucleate cracks normal to the grooves (Figure 12e). Being brittle, these surface oxides are prone to fracture under combined plowing and fatigue loading. The fractured oxide particles then act as hard abrasives within the contact zone. During abrasive wear, large irregular carbides fracture and are subsequently pulled out, further aggravating material loss. Figure 15 provides a schematic illustration of the wear process for Cr12Mo1V1Co steel.

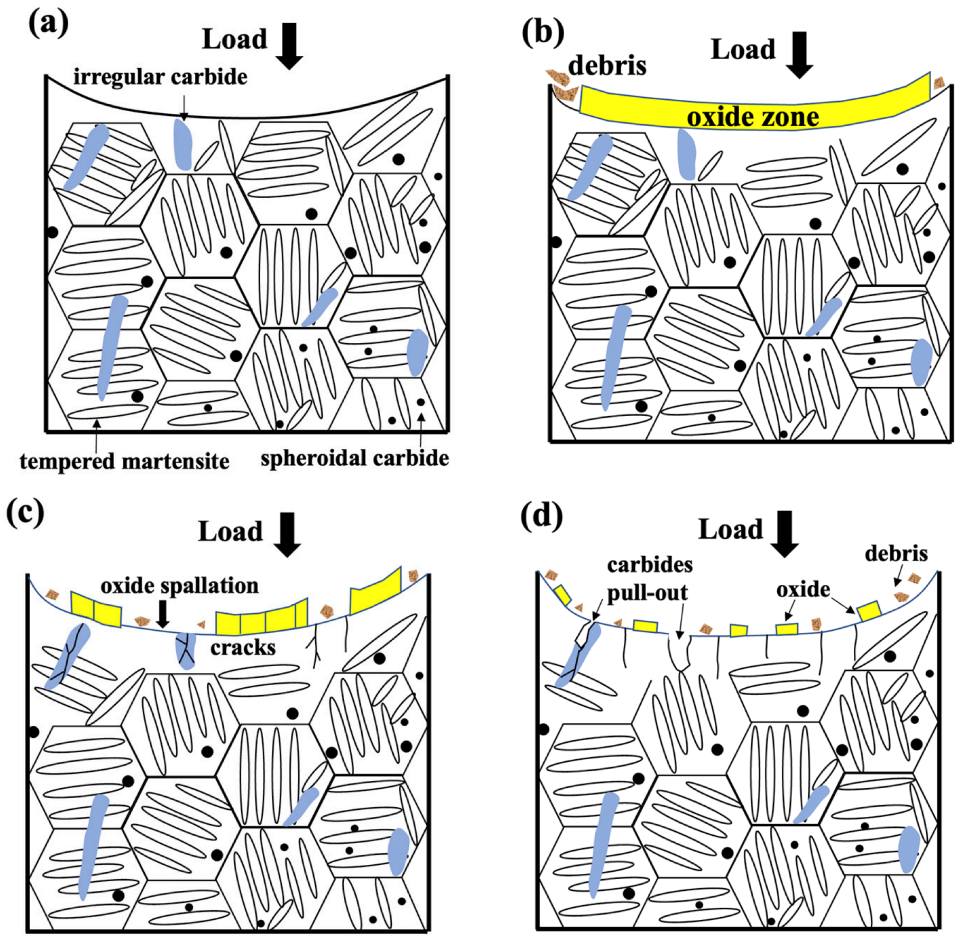


Figure 15. Schematic illustration of wear mechanisms in Cr12Mo1V1Co steel: (**a**) primary abrasive grooves; (**b**) oxide layer formation; (**c**) oxide spallation and carbide cracks; (**d**) carbide pull-out.

4.2. Factors Affecting Wear Rate

4.2.1. Hardness

Figure 16a presents the relationship between the wear rate and the bulk hardness for all heat-treated specimens. A strong negative correlation is observed (Pearson r = −0.82, $p < 0.001$; Spearman ρ = −0.59, $p = 0.021$), although not in a strictly monotonic manner at the individual specimen level. Given that abrasive wear dominates in Cr12Mo1V1Co steel and proceeds via continuous plastic flow, the inferior resistance to plastic deformation of low-hardness specimens results in higher wear rates [25,26,28]. Such low-hardness samples are mainly produced by quenching at 1040–1100 °C followed by tempering at 520 °C, with hardness values of approximately 54 HRC. The reduced hardness stems from more extensive martensite decomposition and pronounced coarsening of secondary carbides at this elevated tempering temperature, as detailed in Section 3.2. An exception is the specimen quenched at 1120 °C and tempered at 480 °C, which exhibits a hardness of 57 HRC yet delivers a relatively low wear rate. XRD analysis (Figure 4d) confirms the presence of retained austenite in this tempered specimen. Das et al. [11] and Singh et al. [28] proposed that the friction-induced transformation of retained austenite into martensite during sliding can compensate for the reduced bulk hardness, thereby leading to a lower wear rate. This interpretation offers a possible explanation for the present experimental results. However, since friction is confined to the contact region, the amount of martensite transformed locally is limited and cannot be verified by bulk XRD measurement. Further experimental verification is currently in progress.

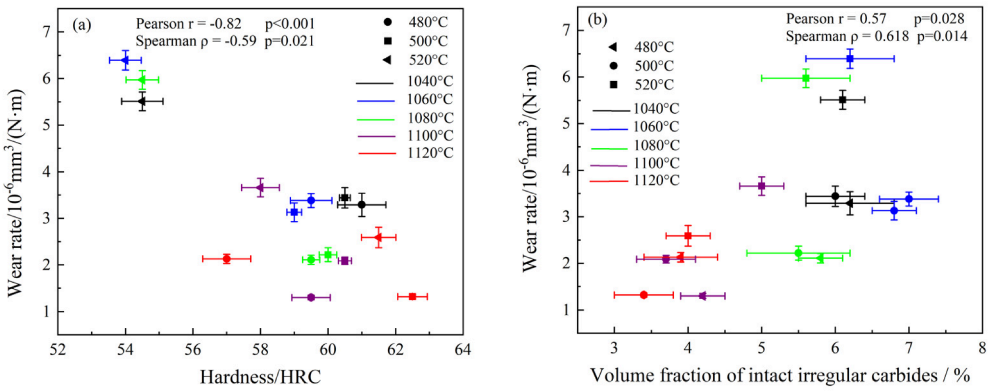


Figure 16. Correlations between the wear rate and (**a**) the bulk hardness and (**b**) the volume fraction of intact irregular carbides.

To provide a mechanical basis for the hardness-dependent wear behavior, the contact stress state under the applied load was evaluated based on Hertzian contact theory [41]. For the ball-on-flat configuration employed in this study, the effective elastic modulus E* of the Si_3N_4 ball (R = 6.35 mm, $E_1 \approx 310$ GPa, $\nu_1 \approx 0.26$ [42]) and the steel substrate ($E_2 \approx 210$ GPa, $\nu_2 \approx 0.30$ [43]) was calculated as:

$$\frac{1}{E^*} = \frac{(1-v_1^2)}{E_1} + \frac{(1-v_2^2)}{E_2} \quad (2)$$

yielding E* ≈ 136 GPa. Under the normal load P = 100 N, the contact radius a and the maximum contact pressure P_0 were then obtained:

$$a = \left(\frac{3PR}{4E^*}\right)^{\frac{1}{3}} \quad (3)$$

$$P_0 = \frac{3P}{2\pi a^2} \quad (4)$$

giving a ≈ 150 μm and p_0 ≈ 2.1 GPa. Under nominal Hertzian contact, the maximum subsurface shear stress, approximately $0.31P_0$ (≈0.65 GPa), remains below the shear yield strength of the steel—approximately half the compressive yield strength, i.e., ~0.9–1.1 GPa over the present hardness range [43], indicating that the nominal contact is essentially elastic. Under actual sliding conditions, however, the near-surface stress is substantially amplified: the tangential friction force shifts the maximum shear stress toward the surface and increases its magnitude when the friction coefficient exceeds approximately 0.3 [41], while local contact at surface asperities and entrapped hard debris generates pressure spikes far exceeding the nominal P_0. Given that the steady-state friction coefficients in this study range from 0.59 to 0.68 (Figure 11), local plastic flow is expected to initiate at the immediate surface, with a greater propensity in the lower-hardness specimens owing to their lower yield strength.

The influence of hardness on the wear rate is also intimately linked to oxidative wear. Morphological analysis reveals that specimens exhibiting elevated wear rates undergo more severe oxide fracture and spallation. Extensive research has established that oxide layers serve as effective barriers separating the metallic substrate from the counterface, thereby reducing the friction coefficient and mitigating material loss [25,44,45]. Conversely, oxide spallation re-exposes the substrate to the wear environment, and the detached oxide debris subsequently acts as three-body abrasives that accelerate metallic plowing. Thus, the correlation between pronounced oxide detachment and elevated wear rates is mechanistically sound.

According to classical oxidative wear models, the wear process under dry sliding conditions involves a cyclic sequence of oxide film formation, growth, fatigue-induced fracture, and spallation. Once the oxide film grows beyond a critical thickness (ξ), it becomes mechanically unstable and fails via fracture under cyclic stress [46,47]. This critical thickness depends intrinsically upon the mechanical properties of the oxide film, the load-bearing capacity of the substrate (e.g., hardness, toughness), and external tribological conditions. In the present study, since all specimens share the same composition and were tested under identical friction conditions (load, sliding speed, counterface material, environment), the mechanical support provided by the substrate to the oxide film emerges as the decisive factor governing its resistance to fatigue-induced detachment. In low-hardness specimens, substantial substrate plastic deformation under contact stresses compels the surface oxide film to accommodate this deformation coordinately, thereby generating elevated tensile stresses within the film. Given the intrinsic brittleness and limited strain tolerance of oxides, cracks readily initiate and propagate rapidly under cyclic loading, culminating in extensive oxide spallation (Figure 14). The resulting hard oxide debris subsequently intensifies plowing of the freshly exposed metallic surface, establishing a self-sustaining cycle of "spallation–plowing–re-oxidation" that markedly accelerates material removal. By contrast, high-hardness specimens provide more stable mechanical support to the oxide film, minimizing additional stresses arising from substrate plastic deformation. Consequently, the oxide film undergoes more gradual, fatigue-mediated spallation, thereby reducing abrasive debris generation and lowering the wear rate. Figure 17 presents the cross-sectional morphologies of wear tracks for the 1080 °C-quenched/520 °C-tempered (54.5 HRC) and 1120 °C-quenched/500 °C-tempered (62.5 HRC) specimens, corresponding to wear rates of 5.97×10^{-6} and 1.32×10^{-6} $mm^3/(N \cdot m)$, respectively. For the low-hardness specimen, the oxide layer is fully spalled, with distinct plastic flow lines and cracks visible adjacent to the worn surface; by contrast, an oxide layer of approximately 1 μm remains on the high-hardness specimen, beneath which martensite laths exhibit negligible deformation. It

is noteworthy that the plastic deformation is confined to the immediate vicinity of the worn surface, which is consistent with the surface-localized maximum shear stress predicted by the sliding contact analysis above. These observations provide direct experimental evidence that the high-hardness matrix mechanically supports the overlying oxide layer through its resistance to plastic deformation.

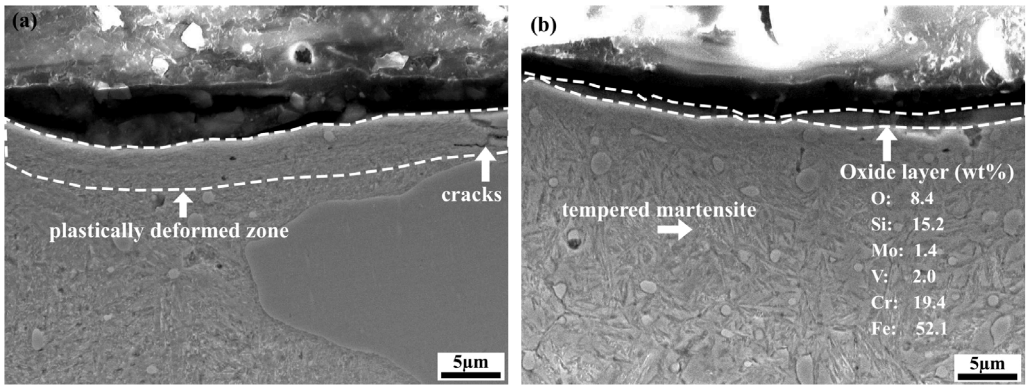


Figure 17. Cross-sectional morphologies of wear tracks for specimens (**a**) quenched at 1080 °C + tempered at 520 °C; (**b**) quenched at 1120 °C + tempered at 500 °C.

4.2.2. Irregular Carbides

Although high hardness is beneficial to the wear resistance, it is not the sole governing factor. For instance, the specimens quenched at 1040–1060 °C and tempered at 480–500 °C exhibit higher wear rates than specimens of comparable hardness quenched at higher temperatures. Examination of the worn morphologies (Figures 12–14) indicates that the response of large irregular carbides during sliding also constitutes an important factor affecting the wear resistance. As shown in Figure 16b, the wear rate exhibits a moderate positive correlation with the volume fraction of intact irregular carbides (Table 3) (Pearson r = 0.57, p = 0.028; Spearman ρ = 0.62, p = 0.014), indicating that a higher fraction of such carbides is associated with accelerated material removal. Accordingly, the wear rates follow the magnitude order: 1120 °C series ≈ 1100 °C series < 1080 °C series < 1060 °C series ≈ 1040 °C series. This is consistent with the progressive dissolution and fragmentation of irregular carbides at elevated quenching temperatures (Figure 5).

The adverse effect of large irregular carbides on the wear rate arises from two coupled processes: carbide fracture, and interface debonding. The sharp corners of irregular carbides induce severe stress concentration under the sliding contact stress field. When the local tensile stress exceeds the fracture strength of the brittle M_7C_3 carbides, cracking occurs within the carbide particles, as evidenced by the cracked carbides in Figure 13e. Meanwhile, the marked mismatch in elastic modulus and plastic deformability between the carbides and the martensitic matrix generates interfacial shear stress during reciprocating sliding. Once the interfacial bonding strength, which is lower than the cohesive strength of the matrix itself, is overcome, the carbide detaches from the matrix and a surface cavity forms (Figure 14e). A similar tendency is observed on the impact fracture surfaces (Section 3.3), where quasi-cleavage facets likewise indicate preferential crack propagation along the carbide/matrix interface. Both processes are doubly detrimental: the resulting cavities directly constitute material loss and act as crack initiation sites for both the oxide film and the substrate, while the detached hard fragments are entrapped at the sliding interface as third-body abrasive particles that further intensify plowing. Similar carbide-mediated damage has been reported for D2 and Cr8 die steels [25,27,33,34]. Elevated quenching temperatures (1100–1120 °C) promote the peripheral fragmentation and partial dissolution of irregular carbides and blunt their sharp corners (Figure 5), thereby suppressing both

processes at the source, which accounts for the lower wear rates of the high-temperature-quenched series.

It is noteworthy that the influence of impact toughness on wear rate is less pronounced than that of hardness and irregular carbides. Samples subjected to quenching at 1040–1080 °C followed by tempering at 520 °C possess the highest toughness yet exhibit the highest wear rates, owing to their insufficient hardness. In contrast, the 1100–1120 °C-quenched series, despite lower toughness, demonstrate superior wear resistance. Nevertheless, within this high-temperature series, samples with better toughness yield consistently lower wear rates.

5. Conclusions

The main outcomes of this study can be briefly highlighted in the following statements.

(1) Elevated quenching temperatures facilitate the dissolution of spheroidal carbides and the preferential edge dissolution of large irregular carbides, generating fine carbide fragments. After triple tempering, martensite transforms into tempered martensite, accompanied by the precipitation of M_7C_3-type spheroidal carbides, which undergo obvious coarsening during 520 °C tempering. Tempering at 480 °C can fully eliminate retained austenite in 1100 °C-quenched samples. In comparison, complete retained austenite elimination for 1120 °C-quenched specimens requires a higher tempering temperature of 500 °C.

(2) Increased retained austenite content and progressive carbide dissolution collectively reduce the as-quenched hardness as the quenching temperature rises. For specimens quenched at 1040–1080 °C, tempering induces a significant reduction in hardness and a notable improvement in impact absorbed energy. By contrast, samples quenched at 1100–1120 °C achieve peak hardness after 500 °C tempering owing to the secondary quenching effect. However, these high-quenched specimens exhibit lower post-tempering impact toughness compared with their low-quenched counterparts.

(3) Under the present experimental conditions, the primary wear mechanisms of Cr12Mo1V1Co steel are abrasive wear, oxidative wear, and fatigue wear. The fracture and pull-out of large irregular carbides constitute an important mechanism of material loss. The wear rate is governed primarily by the matrix hardness, with the volume fraction of intact irregular carbides acting as a secondary, synergistic factor. Specimens subjected to 1100 °C quenching + 480 °C tempering and 1120 °C quenching + 500 °C tempering exhibit the best wear resistance among the investigated heat treatments.

Author Contributions: Conceptualization, J.W.; methodology, B.F.; software, H.G.; validation, J.W. and Y.G.; investigation, J.W., Y.G. and Y.Z.; resources, B.F.; data curation, Y.Z.; writing—original draft preparation, J.W.; writing—review and editing, J.W. and H.G.; visualization, Y.G.; supervision, J.W.; project administration, J.W. and B.F.; funding acquisition, J.W. and B.F. All authors have read and agreed to the published version of the manuscript.

Funding: The present work is funded by Jiangsu Province Industry-University-Research Cooperation Project (BY20251151/DH20250212).

Data Availability Statement: The raw/processed data required to reproduce these findings cannot be shared at this time as the data also forms part of an ongoing study.

Conflicts of Interest: Author Bin Feng was employed by the company Xinyuan Roller Industry Company Limited. The remaining authors declare that the research was conducted in the absence of any commercial or financial relationships that could be construed as a potential conflict of interest.

References

1. Frost, R.E.P.; Lewin, P.L.; Spong, M. An Investigation into the Suitability of Insulated Core Transformer Technology for an Ultra High Voltage Power Supply. *IEEE Trans. Dielectr. Electr. Insul.* **2019**, *26*, 501–507. [CrossRef]
2. Gao, J.; Yang, F.; Han, Y.; Liu, Y.; Sun, H. Structural Design and Magnetic-Vibration Characteristics Analysis of Amorphous Alloy and Oriented Silicon Steel Combined Core. *IEEE Access* **2025**, *13*, 192294–192305. [CrossRef]
3. Zhang, G.; Tang, Z.; Sun, W.; Meng, S.; Wu, K.; Zhang, M.; Zhu, Y. Insulation Coatings for Grain-Oriented Electrical Steel: Mechanisms, Materials, and Future Directions. *Adv. Eng. Mater.* **2026**, *28*, e202501915. [CrossRef]
4. Meng, L.; Tu, Y.; He, C.-X.; Ma, G. Effects of Rolling Passes and Annealing Methods on the Magnetic Properties of Ultrathin Grain-Oriented Silicon Steel. *IET Electron. Mater.* **2025**, *2*, 211–219. [CrossRef]
5. Zhang, N.; Meng, L.; Zhang, B.; Han, Y.; Yang, F.; Ma, G.; Chen, X.; Zhong, S.; Mao, W. Experimental Investigation and Simulation of Crystallographic Orientations Evolution in a Cold-Rolled Ultra-Thin Grain-Oriented Silicon Steel. *J. Magn. Magn. Mater.* **2021**, *517*, 167385. [CrossRef]
6. Abdul Rahim, M.A.S.B.; Minhat, M.B.; Hussein, N.I.S.B.; Salleh, M.S.B. A Comprehensive Review on Cold Work of AISI D2 Tool Steel. *Metall. Res. Technol.* **2018**, *115*, 104. [CrossRef]
7. Fukaura, K.; Yokoyama, Y.; Yokoi, D.; Tsujii, N.; Ono, K. Fatigue of Cold-Work Tool Steels: Effect of Heat Treatment and Carbide Morphology on Fatigue Crack Formation, Life, and Fracture Surface Observations. *Metall. Mater. Trans. A* **2004**, *35*, 1289–1300. [CrossRef]
8. Ghio, E.; Felci, M.; Garziera, R. Effects of Multiple Quenching Treatments on Microstructure and Hardness of O2, D2, and D3 Tool Steels. *J. Manuf. Mater. Process.* **2025**, *9*, 395. [CrossRef]
9. Hua, J.; Pan, J.; Liu, P.; Zhang, G.; Wu, S.; Su, C.; Chen, C.; Zhao, X.; Ren, R. EBSD Study on Proeutectoid Ferrite and Eutectoid Ferrite Refinement Mechanism of D2 Wheel Steel Under a Rolling Condition. *Tribol. Lett.* **2021**, *69*, 148. [CrossRef]
10. Salunkhe, S.; Fabijanic, D.; Nayak, J.; Hodgson, P. Effect of Single and Double Austenitization Treatments on the Microstructure and Hardness of AISI D2 Tool Steel. *Mater. Today Proc.* **2015**, *2*, 1901–1906. [CrossRef]
11. Das, D.; Dutta, A.K.; Toppo, V.; Ray, K.K. Effect of Deep Cryogenic Treatment on the Carbide Precipitation and Tribological Behavior of D2 Steel. *Mater. Manuf. Process.* **2007**, *22*, 474–480. [CrossRef]
12. Dhokey, N.B.; Thakur, C.; Ghosh, P. Influence of Intermediate Cryogenic Treatment on the Microstructural Transformation and Shift in Wear Mechanism in AISI D2 Steel. *Tribol. Trans.* **2021**, *64*, 91–100. [CrossRef]
13. Das, D.; Sarkar, R.; Dutta, A.K.; Ray, K.K. Influence of Sub-Zero Treatments on Fracture Toughness of AISI D2 Steel. *Mater. Sci. Eng. A* **2010**, *528*, 589–603. [CrossRef]
14. Yarasu, V.; Podgornik, B.; Batic, B.S.; Sedlacek, M.; Donik, Č.; Ruiz-Zepeda, F. Microstructure and Mechanical Performance of AISI D2 Tool Steel after Standard and Modified Deep Cryogenic Treatment. *Materialia* **2025**, *41*, 102433. [CrossRef]
15. Torkamani, H.; Raygan, S.; Rassizadehghani, J. Comparing Microstructure and Mechanical Properties of AISI D2 Steel after Bright Hardening and Oil Quenching. *Mater. Des. (1980–2015)* **2014**, *54*, 1049–1055. [CrossRef]
16. Muro, P.; Gimenez, S.; Iturriza, I. Sintering Behaviour and Fracture Toughness Characterization of D2 Matrix Tool Steel, Comparison with Wrought and PM D2. *Scr. Mater.* **2002**, *46*, 369–373. [CrossRef]
17. Mambuscay, C.L.; Ortega-Portilla, C.; Piamba, J.F.; Forero, M.G. Predictive Modeling of Vickers Hardness Using Machine Learning Techniques on D2 Steel with Various Treatments. *Materials* **2024**, *17*, 2235. [CrossRef] [PubMed]
18. Stamenković, U.; Marković, I.; Milanović, P.; Nedeljković, M.; Manasijević, D. The Influence of Heat Treatment on Mechanical, Thermal, and Structural Properties of AISI D2 Steel. *Kov. Mater.* **2024**, *62*, 327–337. [CrossRef]
19. Souid, A.; Mzali, S.; Louhichi, B.; Terres, M.A. Enhancement of Wear Behaviour and Optimization and Prediction of Friction Coefficient of Nitrided D2 Steel at Different Times. *Lubricants* **2025**, *13*, 550. [CrossRef]
20. Buitrago Diaz, J.C.; Ortega-Portilla, C.; Mambuscay, C.L.; Piamba, J.F.; Forero, M.G. Determination of Vickers Hardness in D2 Steel and TiNbN Coating Using Convolutional Neural Networks. *Metals* **2023**, *13*, 1391. [CrossRef]
21. Moretti, M.L.; Recco, A.A.C. Duplex Treatment on AISI D2 Tool Steel: Plasma Nitriding and Reactive Deposition of TiN and TiAlN Films via Magnetron Sputtering. *Matéria (Rio J.)* **2022**, *27*, e20220111. [CrossRef]
22. Liu, X.Y.; Yang, X.; Chen, Z.B.; Guo, C.H.; Li, H.X.; Yang, Z.L.; Dong, T.; Jiang, F.C.; Qiao, Z.H. Microstructure and wear property of laser cladded WC particles reinforced CoCrFeNiMo composite coatings on Cr12MoV steel. *J. Cent. South Univ.* **2025**, *32*, 49–70. [CrossRef]
23. Park, S.J.; Heogh, W.; Yang, J.; Kang, S.; Jeong, W.; Lee, H.; Jang, T.-S.; Jung, H.-D.; Jahazi, M.; Han, S.C.; et al. Meta-Structure of Amorphous-Inspired 65.1Co28.2Cr5.3Mo Lattices Augmented by Artificial Intelligence. *Adv. Compos. Hybrid Mater.* **2024**, *7*, 224. [CrossRef] [PubMed]
24. Ma, X.; Liu, R.; Li, D.Y. Abrasive Wear Behavior of D2 Tool Steel with Respect to Load and Sliding Speed under Dry Sandrrubber Wheel Abrasion Condition. *Wear* **2000**, *241*, 79–85. [CrossRef]
25. Bourithis, L.; Papadimitriou, G.D.; Sideris, J. Comparison of Wear Properties of Tool Steels AISI D2 and O1 with the Same Hardness. *Tribol. Int.* **2006**, *39*, 479–489. [CrossRef]

26. Tang, L.; Gao, C.; Huang, J.; Zhang, H.; Chang, W. Dry Sliding Friction and Wear Behaviour of Hardened AISI D2 Tool Steel with Different Hardness Levels. *Tribol. Int.* **2013**, *66*, 165–173. [CrossRef]
27. Kaba, M.; Filiz, H.I.; Cui, Z.; Baydogan, M.; Cimenoglu, H.; Alpas, A.T. Microstructural Effects on Impact-Sliding Wear Mechanisms in D2 Steels: The Roles of Matrix Hardness and Carbide Characteristics. *Wear* **2024**, *538–539*, 205224. [CrossRef]
28. Singh, K.; Khatirkar, R.K.; Sapate, S.G. Microstructure Evolution and Abrasive Wear Behavior of D2 Steel. *Wear* **2015**, *328–329*, 206–216. [CrossRef]
29. Xiong, S.; Wu, H.; Liu, Z.; Zhang, B. QSAR Models for the Prediction of the Relationship Among Corrosion Inhibition Efficiency, Friction Coefficient and Oil Film Strength of Lubricants. *Polycycl. Aromat. Compd.* **2022**, *42*, 3780–3791. [CrossRef]
30. Xiong, S.; Liang, D.; Zhang, B.; Wu, H.; Mao, X. Tribological Behavior of Mineral and Synthetic Ester Base Oil Containing MoS_2 Nanoparticles. *J. Dispers. Sci. Technol.* **2021**, *42*, 493–502. [CrossRef]
31. He, J.; Xiong, S.; Li, H. Synergistic Lubrication Effect of Graphene Oxide and MoS_2 Nanoparticles in Water-Based Fluid: Experiment and Humid-Environmental MD Simulation Study. *Colloids Surf. A Physicochem. Eng. Asp.* **2025**, *707*, 135900. [CrossRef]
32. Boungomba, H.; Moreau, P.; Sadat, T.; Lilensten, L.; Dubar, M.; Dubar, L. Investigation of the Impact of AISI D2 Tool Steel Wear and Lubrication Type on the Evolution of the Friction Coefficient during Cold Winding Process. *Wear* **2024**, *542–543*, 205272. [CrossRef]
33. Cheng, L.C.; Wu, T.B.; Hu, C.T. The Role of Microstructural Features in Abrasive Wear of a D-2 Tool Steel. *J. Mater. Sci.* **1988**, *23*, 1610–1614. [CrossRef]
34. Shen, X.; Peng, M.; Fu, H.; Wei, T.; Wu, H.; Huang, X.; Li, Z.; Li, L.; Baker, I.; Shan, Q. Enhanced Wear Resistance of a Die Steel via Modification of the M7C3 and M23C6 Carbides. *Wear* **2025**, *576–577*, 206106. [CrossRef]
35. Dumont, M.; Messaadi Ben Said, M.; Lachal, M.; Quidort, D.; Perruchot, M.; Malard, B.; Schell, N.; Maawad, E.; Delagnes, D.; Dehmas, M. In Situ Monitoring of Retained Austenite Decomposition During Tempering of High-Strength Tool Steels. *Metall. Mater. Trans. A* **2025**, *56*, 3481–3494. [CrossRef]
36. Das, D.; Dutta, A.K.; Ray, K.K. Sub-Zero Treatments of AISI D2 Steel: Part I. Microstructure and Hardness. *Mater. Sci. Eng. A* **2010**, *527*, 2182–2193. [CrossRef]
37. Bombac, D.; Fazarinc, M.; Podder, A.S.; Kugler, G. Study of Carbide Evolution During Thermo-Mechanical Processing of AISI D2 Tool Steel. *J. Mater. Eng. Perform.* **2013**, *22*, 742–747. [CrossRef]
38. Fatih, M.R.R.; Chen, H.-J.; Lin, K.-M.; Lin, H.-C. Effect of Tempering Temperature on Carbide Evolution and Mechanical Response of Deep Cryogenically Treated Martensitic Stainless Steel. *Metals* **2025**, *15*, 1152. [CrossRef]
39. Kroon, M.; Faleskog, J. Influence of Crack Deflection into the Carbide/Ferrite Interface on Cleavage Fracture Initiation in Ferritic Steels. *Mech. Mater.* **2008**, *40*, 695–707. [CrossRef]
40. Yapici, A.; Aydin, S.E.; Koc, V.; Kanca, E.; Yildiz, M. Wear Behavior of Borided AISI D2 Steel under Linear Reciprocating Sliding Conditions. *Prot. Met. Phys. Chem. Surf.* **2019**, *55*, 341–351. [CrossRef]
41. Johnson, K.L. *Contact Mechanics*; Cambridge University Press: Cambridge, UK, 1985; ISBN 0-521-25576-7.
42. AZoM. Silicon Nitride (Si_3N_4) Properties and Applications. Available online: https://www.azom.com/properties.aspx?ArticleID=53 (accessed on 5 March 2024).
43. Davis, J.R. (Ed.) *ASM Specialty Handbook: Tool Materials*; ASM International: Materials Park, OH, USA, 1995.
44. Wei, M.X.; Wang, S.Q.; Wang, L.; Cui, X.H.; Chen, K.M. Effect of Tempering Conditions on Wear Resistance in Various Wear Mechanisms of H13 Steel. *Tribol. Int.* **2011**, *44*, 898–905. [CrossRef]
45. Li, S.; Wang, Z.; Cao, Z.; Liu, L.; Wang, Y. Characteristics of Tribo-Oxidation Surface Evolution in Molybdenum–Tungsten–Vanadium Hot-Work Die Steel. *J. Mech. Sci. Technol.* **2024**, *38*, 4097–4104. [CrossRef]
46. Quinn, T.F.J. Review of Oxidational Wear: Part I: The Origins of Oxidational Wear. *Tribol. Int.* **1983**, *16*, 257–271. [CrossRef]
47. Quinn, T.F.J. Review of Oxidational Wear Part II: Recent Developments and Future Trends in Oxidational Wear Research. *Tribol. Int.* **1983**, *16*, 305–315. [CrossRef]

Disclaimer/Publisher's Note: The statements, opinions and data contained in all publications are solely those of the individual author(s) and contributor(s) and not of MDPI and/or the editor(s). MDPI and/or the editor(s) disclaim responsibility for any injury to people or property resulting from any ideas, methods, instructions or products referred to in the content.